Bone hierarchical structure: spatial variation across length scales

Nina K. Wittig and Henrik Birkedal*

Department of Chemistry and iNANO, Aarhus University, 14 Gustav Wieds Vej, Aarhus 8000, Denmark.
*Correspondence e-mail: hbirkedal@chem.au.dk

Bone is a complex hierarchical biomineralized material, which is special amongst biominerals because it is replete with cells, namely, osteocytes. While bone has been scrutinized for centuries, many questions remain open and new research hints that the ultrastructure of bone, encompassing both the bone matrix itself and the embedded cell network, is much more heterogeneous than hitherto realized. A number of these new findings have been made thanks to the enormous developments in X-ray imaging that have occurred in recent decades, and there is promise that they will also allow many of the remaining open questions to be addressed. X-ray absorption or phase imaging affords high three-dimensional (3D) resolution and allows traversing the length scales of bone all the way down to the fine details of the lacuno-canalicular network housing the osteocytes. Multimodal X-ray imaging provides combined information covering both the length scales defined by the size of the measured volume and tomographic resolution, as well as those probed by the signal that is measured. In X-ray diffraction computed tomography (XRD-CT), for example, diffraction signals can be reconstructed tomographically, which offers detailed information about the spatial variations in the crystallographic properties of the bone biomineral. Orientational information can be obtained by tensor tomography. The combination of both small-angle X-ray scattering (SAXS) and wide-angle X-ray scattering (WAXS) tensor tomography gives information on the orientation of bone nanostructure and crystals, respectively. These new technical developments promise that great strides towards understanding bone structure can be expected in the near future. In this review, recent findings that have resulted from X-ray imaging are highlighted and speculation is given on what can be expected to follow.

1. Introduction: bone is a hierarchical living material

Biomineralization, the controlled formation of solids by living organisms, results in a wide range of materials with intriguing properties. These include the nacre of bivalve shells, amorphous silica shells of diatoms and the calcium phosphate-containing bone and teeth of vertebrates (Meyers *et al.*, 2008). Biomineralized structures have solicited the keen interest of researchers for decades because of the exquisite control over the crystallization process exerted by the organisms. Bone is one such biomineral, which is of special interest due to its exceedingly complex structure and the importance of bone for human health, both of which have been studied for many decades (see Reznikov *et al.*, 2016, 2018, and references therein). In the present topical review, we discuss recent findings on bone structure enabled primarily by advances in synchrotron X-ray experimental techniques that together with, for example, advances in transmission electron microscopy (TEM) and other techniques (Reznikov *et al.*, 2016; Goggin *et al.*, 2016), have enabled the field to progress
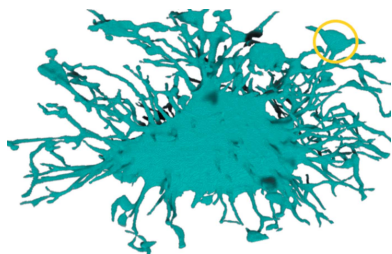
significantly over recent years. As a topical review, this paper will not provide a comprehensive overview of the field and/or experimental techniques but rather focus on a number of selected examples from the very recent literature. The aim of the review is to uncover challenges in bone science ranging from the micro- to the nanoscale, and use the discussed examples to illustrate candidate experimental methods to address them.

1.1. Composition and hierarchies

Bone is formed primarily from collagen fibrils (Fig. 1), nanocrystals with a structure similar to that of hydroxylapatite, water and a number of non-collagenous biological molecules (Reznikov *et al.*, 2014). Bone owes many of its properties, in particular the mechanical ones, to its hierarchical structure. Many hierarchical levels have been described ranging from the atomic-nanoscale to the cm or organ level, as described by many authors (Reznikov *et al.*, 2016; Weiner & Wagner, 1998), with a recent comprehensive update by Reznikov *et al.* (2018); Fig. 1 shows only a selection of these. The main organic component of bone is collagen I that in itself forms a hierarchical structure (Fig. 1). Three collagen molecules assemble into a triple helix that in turn assembles into a collagen microfibril that is fibrilar with a ∼67 nm periodicity. The collagen fibrils are intimately linked with the mineral phase in bone. The crystal system of the mineral is hexagonal, space group $P6_3/m$, and is a hydroxylapatite-like phase heavily substituted by, for example, carbonate. The crystals are often described as having a plate-like morphology (Weiner & Wagner, 1998; Reznikov *et al.*, 2016), seemingly at odds with the hexagonal symmetry of the crystal structure but conceivable if the crystals form under spatial confinement that can modulate crystal growth significantly (Meldrum & O'Shaughnessy, 2020). Recently, high-resolution TEM was used to suggest that the platelets are in fact coherent aggregates of acicular crystals whose morphology is fully consistent with the underlying hexagonal symmetry (Reznikov *et al.*,

2018; Grandfield *et al.*, 2018); the two views are both sketched in Fig. 1. The crystallographic *c* axis of the mineral particles aligns predominantly parallel to the collagen fiber axis to form mineralized collagen fibrils that are 100s of nm in diameter and many μm long. The fibrils arrange in ordered or disordered motifs on the next level of organization and on the μm scale these form collagen fibril bundles (1 μm scale) and lamellae (10 μm scale) that further organize in various motifs depending on the type of bone (skeletal site, organism, maturity stage, *etc.*) on the 100 μm or tissue length scale. In cortical bone, comprising the dense outer shell of long bones in particular, the arrangements depend on the organism as sketched in Fig. 1 and discussed in §2 (*Of mice and men: features of tissue level structure*). Together with strut-like trabecular bone, the cortical bone forms the macroscopic whole bone. Altogether, this corresponds to up to 12 levels of organization (Reznikov *et al.*, 2018) on length scales from ∼10 nm to ∼10 mm, *i.e.* at least six orders of magnitude in length scale, which is highly remarkable. The study of such complex hierarchical materials is challenging. One suitable approach is the use of X-ray imaging techniques that have developed tremendously over the past decade or so, see Withers *et al.* (2021) for an introduction. In particular, the prospects of multimodal and/or multiscale X-ray imaging are exciting, as was recently reported using high-energy synchrotron X-ray phase contrast imaging (Walsh *et al.*, 2021) or by combination of laboratory and synchrotron instrumentation (Wittig *et al.*, 2022) (Fig. 2).

1.2. Cell-laden biomineral

Bone is a rather special biomineral in that a network of cells, the osteocytes, traverses it (Robling & Bonewald, 2020), even if there are animals that have anostoecytic bones (Currey *et al.*, 2017). Osteocytes are housed in lacunae interconnected by canaliculi, together the lacuno-canalicular network. Fig. 3 shows one such lacuna with canaliculi extending from it. The canaliculi are very thin, only a few hundred nm in diameter,
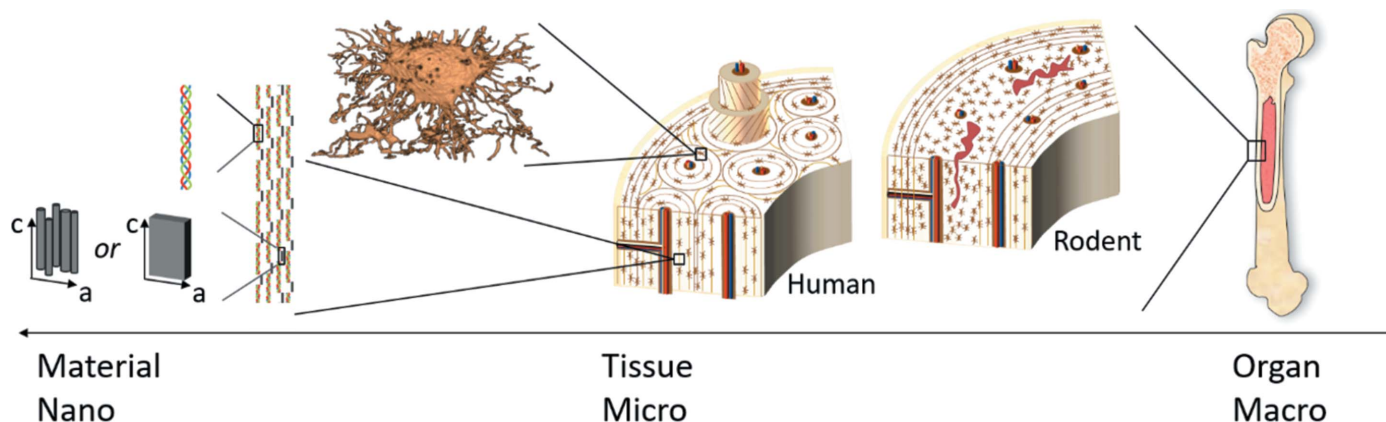

Figure 1
Features of the hierarchical structure of bone going from nano- to macroscopic length scales, with a focus on the dense cortical bone. The main constituents of bone on the nanoscale are mineral crystals, thought to occur as plate-shaped particles, and collagen fibrils. Bone contains cells, osteocytes, housed in lacunae that are 3–12 μm in dimension. In rodent bone, there is a central band of bone formed by a process called endochondral ossification that contains remnant calcified cartilage (red splotches) and has a different osteocyte lacunar density than the surrounding layers of lamellar bone. In humans and some other animals, this is replaced by cylindrical structures called secondary osteons that are formed by Haversian remodelling.

while the ellipsoidal lacunae have dimensions of the order 3 × 7 × 12 µm (Bach-Gansmo *et al.*, 2015), depending on the species. The lacuno-canalicular network thus makes up a complex three-dimensional (3D) structure in itself, and being embedded within the bone matrix, complicates the study of bone structure even further.

In this topical review, we highlight examples of new research in bone structure that indicates that the ultra-structure of bone, encompassing both the bone matrix itself and the embedded lacuno-canalicular network, is much more heterogeneous than hitherto realized. We will first compare and contrast oft-used bone models: humans and rodents at the microscale, which differ significantly in the way they are remodelled, and consequently in the bone and cell organiza-tion. We then discuss the cellular network in bone in more detail followed by experiments targeting the spatial variation in bone crystallography or in orientation at both the nano- and crystallographic scale. We hope that the review will stimulate others to employ the described, and/or alternative, methods to help tackle the many open, but fascinating, challenges in bone biomineralization research.

2. Of mice and men: features of tissue level structure

Different species display different bone structures on the microscale (Fig. 1). Humans and some other animals undergo Haversian remodelling of the long bones. In this process, cells dig channels into the bone, which are subsequently filled from the outside in to form secondary osteons (Fig. 1) (see, for example, Wittig, Palle *et al.*, 2019, and references therein). Other species do not undergo Haversian remodelling. This includes rats and mice (Figs. 1 and 2). The long bones of these species therefore largely stem from endochondral ossification. Endochondral ossification, which also takes place in humans, is the process of long bone growth starting from a cartilagious growth plate in which cartilage is gradually mineralized and then replaced by bone. During further growth, bone is both removed and added from the surfaces of the long bone. Since rodents do not present Haversian remodelling, their long bones contain both such appositional lamellar bone and remnant bone from the endochondral ossification. This remnant bone contains residual calcified cartilage (Bach-Gansmo *et al.*, 2013) and displays a higher osteocyte density than the appositional bone. The lacunar orientation is much more strongly aligned with the bone long axis in the apposi-tional bone than in the central endochondrally derived bone (Bach-Gansmo *et al.*, 2015; Birkedal, 2022). This correlation between lacunar geometric properties with the type of bone housing the cells indicates a strong coupling across length scales and that the local mineralization mechanisms become reflected in the whole bone. Evidently, it also points to differences between human bone and the widely used rodent models, something that we as researchers should be aware of when employing such models.

3. Nanoscale features of the osteocyte lacuno-canalicular network

The cellular network in bone is challenging to study in the full context of the biomineralized tissue since the cells are entombed in the poorly transparent bone matrix (Goggin *et al.*, 2016). X-ray imaging is in principle well suited for this purpose (Palle *et al.*, 2019; Wittig *et al.*, 2022), as illustrated in Fig. 2, but have only over the past decade or two reached resolutions that allow mapping of the full network, including the 100s of nm wide canaliculi. Recent studies using phase-based X-ray imaging in the form of ptychography (Dierolf *et al.*, 2010; Zanette *et al.*, 2015) and holotomography thus mapped nanoscale features of the cellular network (Hesse *et al.*, 2014; Pacureanu *et al.*, 2012; Langer *et al.*, 2012; Wittig, Laugesen *et al.*, 2019; Wittig, Birkbak *et al.*, 2019). Alter-natively, scanning electron microscopy (SEM) (Shah *et al.*,
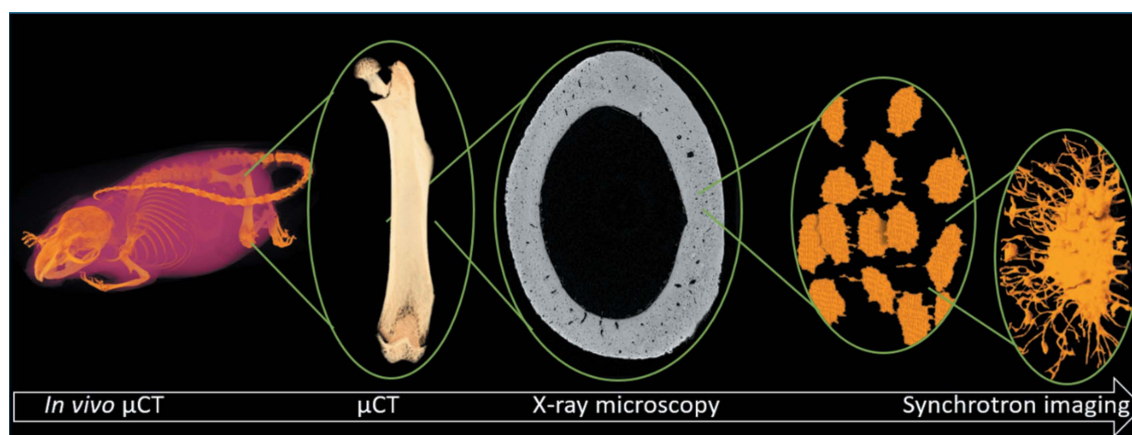

Figure 2
Illustration of the use of multiscale imaging combining different instrumentation ranging from whole animal imaging (rendered mouse is 8.7 cm from nose to start of tail) with *in vivo* µCT (or clinical CT for humans) over laboratory µCT to map individual bones/bone pieces (rendered mouse femur is 16 mm long) to higher resolution in-house X-ray microscopy that reveals interior structure (reconstructed cross section of mouse mid-femur is 1.9 mm from top to bottom), including osteocyte lacunae typically 10–15 µm long, to synchrotron imaging that can be conducted in high throughput sub-µm resolution mode to investigate large volumes and a large number of specimens or in nanotomography mode to reveal fine details, such as the canaliculi of the lacuno-canalicular network (length of the rendered mouse osteocyte lacuna is 15 µm). Adapted from data reported in Wittig *et al.* (2022).

2019), in particular, 3D focussed ion beam SEM (FIB-SEM) imaging (Weiner *et al.*, 2021), atomic force microscopy (AFM), that additionally affords local mechanical information (Rux *et al.*, 2022; Zhang *et al.*, 2015), or confocal laser scanning microscopy (CLSM) on dye infused bone (Kerschnitzki *et al.*, 2011, 2013; van Tol *et al.*, 2020), have been very useful. On larger length scales, where focus is mainly on osteocyte lacunae, both laboratory and synchrotron 3D X-ray imaging is useful (Wittig *et al.*, 2022) (Fig. 2). With synchrotron radiation it is possible to investigate a large amount of samples and/or large sample volumes to afford statistical information, which is essential for reaching conclusions of biological relevance (Hoac *et al.*, 2020; Bach-Gansmo, Wittig *et al.*, 2016; Bach-Gansmo, Brüel *et al.*, 2016).

3.1. Canalicular junctions

The very high spatial resolution afforded by synchrotron X-ray imaging recently revealed new features of the osteocyte lacuno-canalicular network (Wittig, Laugesen *et al.*, 2019). Fig. 3 shows a single osteocyte lacuna excised *in silico* from a larger data set. The lacuna has a plethora of canaliculi emanating from it. The network is observed to be surprisingly bulgy and in some places several canaliculi cross in a void space that was named a canalicular junction. The canalicular junctions could only be discovered through the 3D nature of the holotomographic data set and had eluded detection over decades of high-resolution two-dimensional (2D) analyses. This highlights the importance of investigating hierarchical materials in 3D.

To determine whether the canalicular junctions were connected to the fluid network of the lacuno-canalicular network in bone, additional experiments were required: to this end the confocal imaging methods pioneered by Fratzl and co-workers (Kerschnitzki *et al.*, 2011, 2013; van Tol *et al.*, 2020) were harnessed. In this technique, a dye is infused into the cellular network and imaged by confocal microscopy. From this it was found that (1) the canalicular junctions were indeed connected to the fluid network and (2) they appear in mice, humans, cows and rats (Wittig, Laugesen *et al.*, 2019). The observation that the canalicular junctions are connected to the fluid network is important, since osteocytes are believed to sense stress on the bone *via* changes in the shear flow forces in the lacuno-canalicular network (Robling & Bonewald, 2020). Fluid flow simulations on highly simplified and reduced model lacuno-canalicular networks with or without canalicular junctions showed that the presence of canalicular junctions indeed changes the fluid flow within the network. Simulations of more realistic models of the lacuno-canalicular network will, however, be needed to fully evaluate the importance of canalicular junctions for the fluid flow dynamics in bone.

4. Bone mineral: one size does not fit all

Traditional 3D X-ray imaging as described above gives information on material density but not directly on the crystallographic properties of the material. Attaining such information requires X-ray diffraction (XRD) information. Given the complex hierarchical nature of bone, it may be hypothesized that the crystallographic properties also vary spatially, *e.g.* with local variations in oligoelement concentration, mechanic deformation and/or spatial variation in the composition of the organic matrix. Ideally, one would require spatially resolved XRD information to test this hypothesis. To this end, XRD can be collected in tomographic mode using a pencil X-ray beam (Birkbak *et al.*, 2015). The use of this technique, called XRD-CT or DSCT, took off after it was first demonstrated using synchrotron radiation on bone (Stock *et al.*, 2008), followed shortly thereafter by applications to other materials (Bleuet *et al.*, 2008). Scattering angle (2θ) dependent reconstruction yields full XRD patterns in each voxel, which

osteon canal

Figure 4
Apparent crystallite size along the crystallographic *c* axis as a function of position perpendicular to the osteon canal determined by X-ray diffraction computed tomography (XRD-CT). The image represents an average over the 10.4 µm height of the sample volume. Small crystallites (light tones) are observed close to the osteon canal. The scale bar is 20 µm. Adapted from data in Wittig, Palle *et al.* (2019).
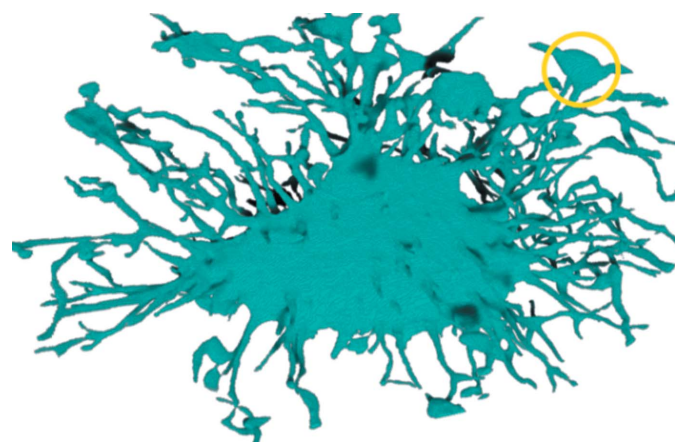

Figure 3
A single osteocyte lacuna (15 µm long) with surrounding canaliculi extracted from a 3D synchrotron nano-holotomography data set (Wittig, Laugesen *et al.*, 2019). The yellow circle highlights a canalicular junction.
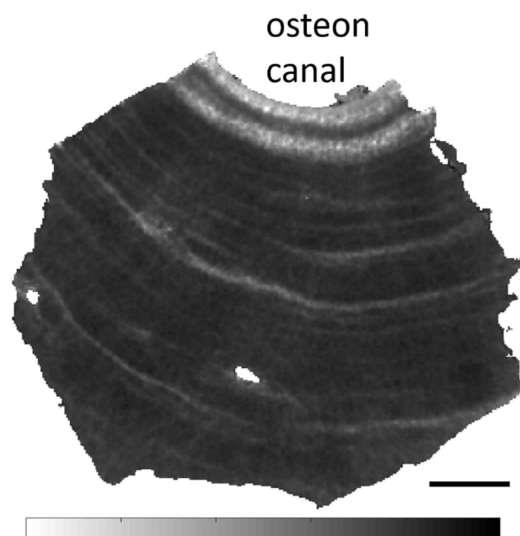
have for example been used to identify polymorph distributions in complex biominerals and even estimate local substitution chemistry from shifts in diffraction peak positions (Leemreize *et al.*, 2013). The resolution of these measurements is ultimately limited by the available beam size and has only recently surpassed a µm (*vide infra*), which would be necessary to probe many of the potential variations in bone described above. Using nano-focused hard X-ray beams, a true 3D resolution of better than 120 nm has now been achieved in a multimodal experiment incorporating both diffraction and fluorescence information on bone (Palle *et al.*, 2020).

4.1. Varying mineral properties across human osteonal bone

The ability to spatially resolve crystallographic information in 3D by XRD-CT allowed hitherto unanswered questions about bone structure to be addressed (Wittig, Palle *et al.*, 2019). With the aim of resolving information across single bone lamellae, an X-ray beam of 0.4 µm diameter was used. A pseudo-octagonal sample of human cortical bone about 130 µm in diameter and cut with one of the sides defined by an osteon canal, was measured by XRD-CT. The data were reconstructed to result in over 3.6 million diffraction patterns, each of which was analysed by Rietveld refinement using an automation approach developed by Frølich & Birkedal (2015).

Analysis of the Rietveld results showed that the data varied remarkably little over the 10.4 µm height of the sampled volume. Fig. 4 shows the apparent crystallite length along the *c* axis obtained by height-averaging the results. The apparent crystallite length was obtained from the broadening of the diffraction peaks, not separating crystallite size effects from possible microstrain fluctuations. The crystallites were found to be smaller close to the osteon canal both along the *c* axis (Fig. 4) and perpendicular thereto. Similar observations were obtained by SAXS in rabbits where the mineral thickness was smaller close to the osteon canal than further away (Törnquist *et al.*, 2020). These observations indicate that bone biomineral crystallization is under strict spatial control. Indeed the composition of the organic matrix, which is known to affect the mineralization process, varies spatially. Mineralization in bone is under negative (inhibiting) control (McKee *et al.*, 2022). One such inhibitor is osteopontin. In normal mineralization, osteopontin is degraded under the control of the PHEX gene. Defects therein lead to disease, called crosslinked hypophosphatemia in humans, which is characterized by mineralization defects. It also results in enlarged osteocyte lacunae and unmineralized halos around these, as well as unmineralized halos around osteon canals (Hoac *et al.*, 2020). We therefore hypothesized that the smaller crystallites observed by XRD-CT, result from inhibition of crystallite
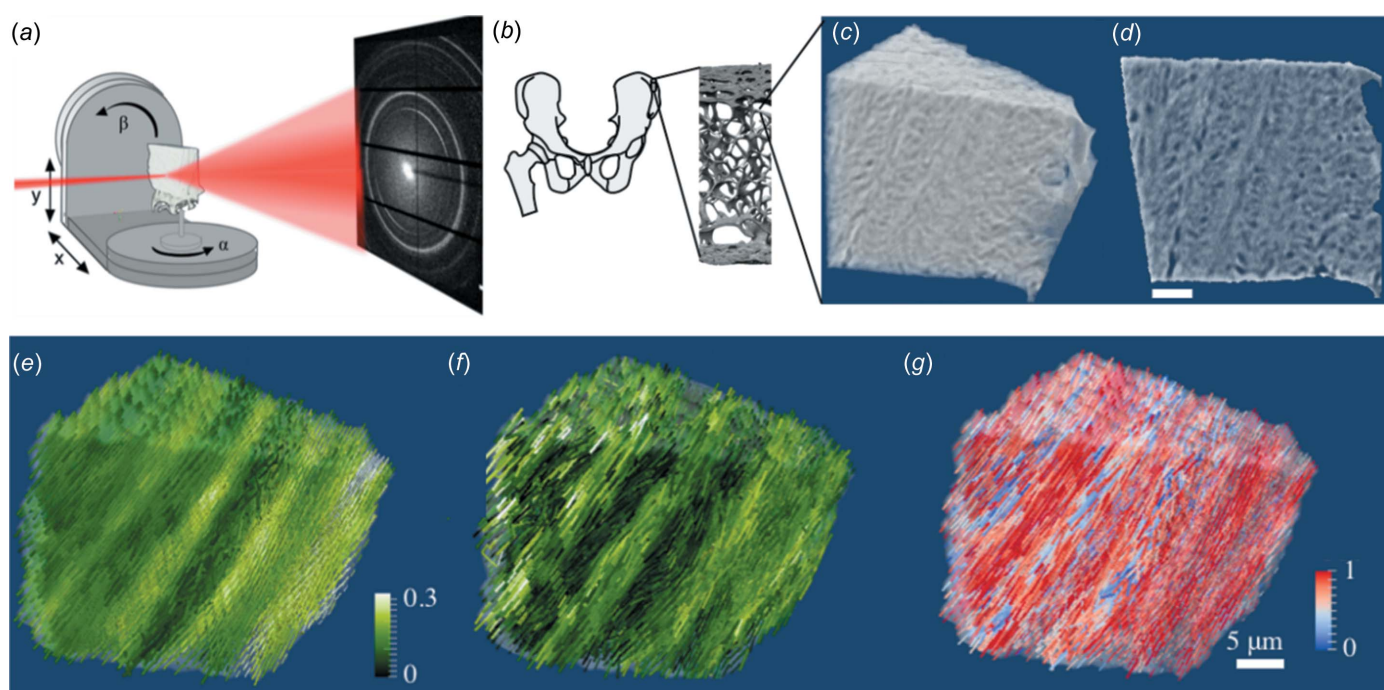

Figure 5
Tensor tomography reveals orientation in 3D. (*a*) The principle behind combined SAXS and WAXS tensor tomography. The sample is raster scanned through a pencil X-ray beam and scattering data are collected as a function of position (x, y), rotation angle (α) and tilt angle (β). (*b*) The bone sample under study was taken from the human iliac crest and a small cuboid sample was cut as indicated. (*c*)/(*d*) The structure of the sample was studied by high-resolution synchrotron tomography. The tomographic 3D data (*c*) were oriented into the same orientation as the tensor tomography data shown in parts (*e*)–(*g*) and a slice through the centre of the volume was virtually extracted in which the traces of the mineralized collagen fibrils can be seen in part (*d*). The scale bar in part (*d*) is 5 µm. (*e*) Results of SAXS tensor tomography in the same cut volume as in part (*c*). Each voxel is represented by a line, the orientation of which gives the dominant orientation of the nanoscale features. The degree of orientation is indicated by the colour scheme. (*f*) Results from WAXS tensor tomography based on the (002) reflection; symbols and colour scale are the same as in part (*e*). (*g*) Co-orientation analysis with red signifying perfect alignment of the WAXS (002) tensor results and the SAXS nanoscale tensor results, while blue represents opposite alignment. Note the appearance of blue bands of bone voxels that do not display co-alignment. Adapted from Grünewald *et al.* (2020).

growth by, for example, osteopontin fragments (Wittig, Palle *et al.*, 2019). This would suggest that mineral crystals around osteocyte lacunae may also be expected to be smaller in size; the ability to test this hypothesis can be expected to emerge as ~100 nm spatial resolution XRD studies become possible (Palle *et al.*, 2020).

4.2. New insights on the orientation of bone mineral and nanostructure

The mesoscale structures of bone can be investigated by small-angle X-ray scattering (SAXS) as especially pioneered by Fratzl (see Fratzl *et al.*, 1991; Bünger *et al.*, 2010, and references therein). However, 2D scanning SAXS can only provide projected information on the orientation of nanoscale features, typically interpreted as reflecting the orientation of mineralized collagen fibrils. This is problematic given the complex 3D structure of bone. SAXS tomography does not solve this problem since information remains hidden when only rotating the sample around one axis because a cone volume around the rotation axis is not accessed. Instead, the sample must also be tilted (Guizar-Sicairos *et al.*, 2020; Liebi *et al.*, 2015, 2018; Schaff *et al.*, 2015). Thereby it becomes possible to map the main orientation of nanoscale features in 3D. In such an experiment, called SAXS tensor tomography, the sample is raster scanned through a pencil X-ray beam as a function of rotation (α) for a number of sample tilt angles (β), as shown in Fig. 5(*a*). The orientational information can, for example, be fitted to an expansion in surface spherical harmonics. The approach provides information on two length scales: the mesoscopic from SAXS and the tomographic determined by the voxel size in the experiment, typically the beam size. For example, SAXS tensor tomography provided information on the 3D organization of bone forming around degrading ZX10 magnesium implants in rats (Liebi *et al.*, 2021).

We recently harnessed tensor tomography to investigate the organization of human lamellar bone (Grünewald *et al.*, 2020) with the aim of probing not only the orientation of nanostructural features but also that of the mineral phase. To this end, the method was extended to diffraction signals and the orientation of the *c* axis was obtained by XRD tensor tomography based on the (002) reflection of apatite. A piece of human lamellar bone from the iliac crest was studied by both synchrotron tomography [Figs. 5(*b*)–5(*d*)] and combined SAXS and WAXS tensor tomography. To allow resolving the bone lamellae, a 1 µm hard X-ray beam was used in the latter. The synchrotron tomography allowed the resolution of collagen fibril patterns within lamellae, as seen both in the cut cube and the cross section through the 3D volume shown in Figs. 5(*c*) and 5(*d*). Figs. 5(*e*) and 5(*f*) show reconstructed orientational information in the analysed bone cube, with the direction of each line giving the orientation of nanostructure and crystallographic *c* axis from, respectively, SAXS and WAXS, and the colour indicating the degree of orientation. The currently accepted models of bone structure predict that the *c* axis should be aligned with the nanoscale features. This

would mean that the (002) reflection should be perpendicular to the SAXS signal from the collagen fibril cross section so that the orientational information in Figs. 5(*e*) and 5(*f*) should be coaligned. This is indeed observed for most of the voxels. However, the analysis revealed that there are bands where this alignment is not as large as expected. This is illustrated in Fig. 5(*g*), which shows a co-orientation measure ranging from 1 for fully aligned (red) to 0 for fully misaligned (blue). The blue bands indicate that there are zones of misorientation possibly resulting from an additional mineral component not aligned with the collagen fibrils even if this requires further confirmation.

WAXS tensor tomography was recently implemented for high energy X-rays of 50 keV, where a bone sample of about 3 mm^3 was analysed with a beam size of 50 µm (Mürer *et al.*, 2021). The authors analysed the bone formation front in a piglet growth plate, *i.e.* the process of endochondral ossification (*vide supra*). They found that the crystallographic *c* axis was predominantly orientated towards the ossification front close to the growth cartilage, indicating that patterns of more or less co-alignment emerge at several length scales. These experiments suggest that WAXS tensor tomography can become a powerful technique especially as synchrotron upgrades provide access to higher flux and higher energies to reduce measurement time or increase resolution and decrease the risk of beam damage, respectively.

5. Future directions

While great strides have been made towards understanding bone structure and how it is regulated, some of which have been discussed above, many outstanding questions remain. Some of these include the exact nature of the mineral crystals around the osteocyte lacuno-canalicular network, bone formation, the 3D orientation of bone and how it is regulated during growth and/or implant fixation, and the relation of all these factors to bone mechanics. The technical developments in methods to study bone, including X-ray imaging, scattering and diffraction methods, promise that it will be possible to address several of these challenges in the coming years even if possible beam damage effects must be considered carefully, for example by careful choice of X-ray energy and/or the design of experiments that reduce the delivered X-ray dose. The coming decade of bone science will thus be as surprising and interesting as the last one.

past and present. We also thank the various synchrotron sources involved in the work; we acknowledge especially the Paul Scherrer Institut, Villigen, Switzerland, for provision of synchrotron radiation beamtime at the TOMCAT beamline X02DA of the SLS, the European Synchrotron Radiation Facility for provision of synchrotron radiation facilities at beamlines ID13 and ID16a, and DESY (Hamburg, Germany), a member of the Helmholtz Association HGF, for the provision of experimental facilities at beamline P06 at PETRA III.

References

Bach-Gansmo, F. L., Brüel, A., Jensen, M. V., Ebbesen, E. N., Birkedal, H. & Thomsen, J. S. (2016). *Bone*, **91**, 11–19.

Bach-Gansmo, F. L., Irvine, S. C., Brüel, A., Thomsen, J. S. & Birkedal, H. (2013). *Calcif. Tissue Int.* **92**, 330–338.

Bach-Gansmo, F. L., Weaver, J. C., Jensen, M. H., Leemreize, H., Mader, K. S., Stampanoni, M., Brüel, A., Thomsen, J. S. & Birkedal, H. (2015). *J. Struct. Biol.* **191**, 59–67.

Bach-Gansmo, F. L., Wittig, N. K., Brüel, A., Thomsen, J. S. & Birkedal, H. (2016). *Bone*, **91**, 139–147.

Birkbak, M. E., Leemreize, H., Frølich, S., Stock, S. R. & Birkedal, H. (2015). *Nanoscale*, **7**, 18402–18410.

Birkedal, H. (2022). *Calcif. Tissue Int.* **110**, 143.

Bleuet, P., Welcomme, E., Dooryhée, E., Susini, J., Hodeau, J.-L. & Walter, P. (2008). *Nat. Mater.* **7**, 468–472.

Bünger, M. H., Oxlund, H., Hansen, T. K., Sørensen, S., Bibby, B. M., Thomsen, J. S., Langdahl, B. L., Besenbacher, F., Pedersen, J. S. & Birkedal, H. (2010). *Calcif. Tissue Int.* **86**, 294–306.

Currey, J. D., Dean, M. N. & Shahar, R. (2017). *Biol. Rev.* **92**, 1702–1719.

Dierolf, M., Menzel, A., Thibault, P., Schneider, P., Kewish, C. M., Wepf, R., Bunk, O. & Pfeiffer, F. (2010). *Nature*, **467**, 436–439.

Fratzl, P., Fratzl-Zelman, N., Klaushofer, K., Vogl, G. & Koller, K. (1991). *Calcif. Tissue Int.* **48**, 407–413.

Frølich, S. & Birkedal, H. (2015). *J. Appl. Cryst.* **48**, 2019–2025.

Goggin, P. M., Zygalakis, K. C., Oreffo, R. O. C. & Schneider, P. (2016). *Eur. Cell. Mater.* **31**, 264–295.

Grandfield, K., Vuong, V. & Schwarcz, H. P. (2018). *Calcif. Tissue Int.* **103**, 606–616.

Grünewald, T. A., Liebi, M., Wittig, N. K., Johannes, A., Sikjaer, T., Rejnmark, L., Rosenthal, M., Guizar-Sicairos, M., Birkedal, H. & Burghammer, M. (2020). *Sci. Adv.* **6**, eaba4171.

Guizar-Sicairos, M., Georgiadis, M. & Liebi, M. (2020). *J. Synchrotron Rad.* **27**, 779–787.

Hesse, B., Varga, P., Langer, M., Pacureanu, A., Schrof, S., Männicke, N., Suhonen, H., Maurer, P., Cloetens, P., Peyrin, F. & Raum, K. (2015). *J. Bone Miner. Res.* **30**, 346–356.

Hoac, B., Østergaard, M., Wittig, N. K., Boukpessi, T., Buss, D. J., Chaussain, C., Birkedal, H., Murshed, M. & McKee, M. D. (2020). *J. Bone Miner. Res.* **35**, 2032–2048.

Kerschnitzki, M., Kollmannsberger, P., Burghammer, M., Duda, G. N., Weinkamer, R., Wagermaier, W. & Fratzl, P. (2013). *J. Bone Miner. Res.* **28**, 1837–1845.

Kerschnitzki, M., Wagermaier, W., Roschger, P., Seto, J., Shahar, R., Duda, G. N., Mundlos, S. & Fratzl, P. (2011). *J. Struct. Biol.* **173**, 303–311.

Langer, M., Pacureanu, A., Suhonen, H. Q. G., Grimal, Q., Cloetens, P. & Peyrin, F. (2012). *PLoS One*, **7**, e35691.

Leemreize, H., Almer, J. D., Stock, S. R. & Birkedal, H. (2013). *J. R. Soc. Interface*, **10**, 20130319.

Liebi, M., Georgiadis, M., Kohlbrecher, J., Holler, M., Raabe, J., Usov, I., Menzel, A., Schneider, P., Bunk, O. & Guizar-Sicairos, M. (2018). *Acta Cryst.* A**74**, 12–24.

Liebi, M., Georgiadis, M., Menzel, A., Schneider, P., Kohlbrecher, J., Bunk, O. & Guizar-Sicairos, M. (2015). *Nature*, **527**, 349–352.

Liebi, M., Lutz-Bueno, V., Guizar-Sicairos, M., Schönbauer, B. M., Eichler, J., Martinelli, E., Löffler, J. F., Weinberg, A., Lichtenegger, H. & Grünewald, T. A. (2021). *Acta Biomater.* **134**, 804–817.

McKee, M. D., Buss, D. J. & Reznikov, N. (2022). *J. Struct. Biol.* **214**, 107823.

Meldrum, F. C. & O'Shaughnessy, C. (2020). *Adv. Mater.* **32**, 2001068.

Meyers, M. A., Chen, P.-Y., Lin, A. Y.-M. & Seki, Y. (2008). *Prog. Mater. Sci.* **53**, 1–206.

Mürer, F. K., Chattopadhyay, B., Madathiparambil, A. S., Tekseth, K. R., Di Michiel, M., Liebi, M., Lilledahl, M. B., Olstad, K. & Breiby, D. W. (2021). *Sci. Rep.* **11**, 2144.

Pacureanu, A., Langer, M., Boller, E., Tafforeau, P. & Peyrin, F. (2012). *Med. Phys.* **39**, 2229–2238.

Palle, J., Wittig, N. K., Kubec, A., Niese, S., Rosenthal, M., Burghammer, M., Grünewald, T. A. & Birkedal, H. (2020). *J. Struct. Biol.* **212**, 107631.

Palle, J., Wittig, N. K., Østergaard, M., Jensen, A. B. & Birkedal, H. (2019). *Proc. SPIE*, **11113**, 1111316.

Reznikov, N., Bilton, M., Lari, L., Stevens, M. M. & Kröger, R. (2018). *Science*, **360**, aao2189.

Reznikov, N., Shahar, R. & Weiner, S. (2014). *Acta Biomater.* **10**, 3815–3826.

Reznikov, N., Steele, J. A. M., Fratzl, P. & Stevens, M. M. (2016). *Nat. Rev. Mater.* **1**, 16041.

Robling, A. G. & Bonewald, L. F. (2020). *Annu. Rev. Physiol.* **82**, 485–506.

Rux, C. J., Vahidi, G., Darabi, A., Cox, L. M. & Heveran, C. M. (2022). *Bone*, **157**, 116327.

Schaff, F., Bech, M., Zaslansky, P., Jud, C., Liebi, M., Guizar-Sicairos, M. & Pfeiffer, F. (2015). *Nature*, **527**, 353–356.

Shah, F. A., Ruscsák, K. & Palmquist, A. (2019). *Bone Res.* **7**, 15.

Stock, S. R., De Carlo, F. & Almer, J. D. (2008). *J. Struct. Biol.* **161**, 144–150.

Tol, A. F. van, Schemenz, V., Wagermaier, W., Roschger, A., Razi, H., Vitienes, I., Fratzl, P., Willie, B. M. & Weinkamer, R. (2020). *PNAS*, **117**, 32251–32259.

Törnquist, E., Isaksson, H. & Turunen, M. J. (2020). *J. Bone Miner. Metab.* **38**, 289–298.

Walsh, C. L., Tafforeau, P., Wagner, W. L., Jafree, D. J., Bellier, A., Werlein, C., Kühnel, M. P., Boller, E., Walker-Samuel, S., Robertus, J. L., Long, D. A., Jacob, J., Marussi, S., Brown, E., Holroyd, N., Jonigk, D. D., Ackermann, M. & Lee, P. D. (2021). *Nat. Methods*, **18**, 1532–1541.

Weiner, S., Raguin, E. & Shahar, R. (2021). *Nat. Rev. Endocrinol.* **17**, 307–316.

Weiner, S. & Wagner, H. D. (1998). *Annu. Rev. Mater. Sci.* **28**, 271–298.

Withers, P. J., Bouman, C., Carmignato, S., Cnudde, V., Grimaldi, D., Hagen, C. K., Maire, E., Manley, M., Du Plessis, A. & Stock, S. R. (2021). *Nat. Rev. Methods Primers*, **1**, 18.

Wittig, N. K., Birkbak, M. E., Bach-Gansmo, F. L., Pacureanu, A., Wendelboe, M. H., Brüel, A., Thomsen, J. S. & Birkedal, H. (2019). *Calcif. Tissue Int.* **105**, 308–315.

Wittig, N. K., Laugesen, M., Birkbak, M. E., Bach-Gansmo, F. L., Pacureanu, A., Bruns, S., Wendelboe, M. H., Brüel, A., Sørensen, H. O., Thomsen, J. S. & Birkedal, H. (2019). *ACS Nano*, **13**, 6421–6430.

Wittig, N. K., Østergaard, M., Palle, J., Christensen, T. E. K., Langdahl, B. L., Rejnmark, L., Hauge, E.-M., Brüel, A., Thomsen, J. S. & Birkedal, H. (2022). *J. Struct. Biol.* **214**, 107822.

Wittig, N. K., Palle, J., Østergaard, M., Frølich, S., Birkbak, M. E., Spiers, K., Garrevoet, J. & Birkedal, H. (2019). *ACS Nano*, **13**, 12949–12956.

Zanette, I., Enders, B., Dierolf, M., Thibault, P., Gradl, R., Diaz, A., Guizar-Sicairos, M., Menzel, A., Pfeiffer, F. & Zaslansky, P. (2015). *Sci. Rep.* **5**, 9210.

Zhang, S., Bach-Gansmo, F. L., Xia, D., Besenbacher, F., Birkedal, H. & Dong, M. (2015). *Nano Res.* **8**, 3250–3260.